Inverse Monte Carlo for estimation of scattering and absorption in liquid optical phantoms

Hanna Karlsson, Ingemar Fredriksson, Marcus Larsson and Tomas Strömberg

Linköping University Post Print

N.B.: When citing this work, cite the original article.

Inverse Monte Carlo for estimation of scattering and absorption in liquid optical phantoms

Hanna Karlsson,[1,*] Ingemar Fredriksson,[1,2] Marcus Larsson,[1] and Tomas Strömberg[1]

[1]Department of Biomedical Engineering, Linköping University, S-581 85 Linköping, Sweden
[2]Perimed AB, Datavägen 9A, S-175 43 Järfälla, Stockholm, Sweden
[*]hanna.karlsson@liu.se

Abstract: A spectroscopic probe with multiple detecting fibers was used for quantifying absorption and scattering in liquid optical phantoms. The phantoms were mixtures of Intralipid and red and blue food dyes. Intensity calibration for the detecting fibers was undertaken using either a microsphere suspension (absolute calibration) or a uniform detector illumination (relative calibration between detectors). Two different scattering phase functions were used in an inverse Monte Carlo algorithm. Data were evaluated for residual spectra (systematic deviations and magnitude) and accuracy in estimation of scattering and absorption. Spectral fitting was improved by allowing for a 10% intensity relaxation in the optimization algorithm. For a multi-detector setup, non-systematic residual spectrum was only found using the more complex Gegenbauer-kernel phase function. However, the choice of phase function did not influence the accuracy in the estimation of absorption and scattering. Similar estimation accuracy as in the multi-detector setup was also obtained using either two relative calibrated detectors or one absolute calibrated detector at a fiber separation of 0.46 mm.

References and links

1. R. Richards-Kortum and E. Sevick-Muraca, "Quantitative optical spectroscopy for tissue diagnosis," Annu. Rev. Phys. Chem. **47**(1), 555–606 (1996).
2. T. J. Farrell, M. S. Patterson, and B. Wilson, "A diffusion theory model of spatially resolved, steady-state diffuse reflectance for the noninvasive determination of tissue optical properties in vivo," Med. Phys. **19**(4), 879–888 (1992).
3. J. L. Hollmann and L. V. Wang, "Multiple-source optical diffusion approximation for a multilayer scattering medium," Appl. Opt. **46**(23), 6004–6009 (2007).
4. F. Bevilacqua and C. Depeursinge, "Monte Carlo study of diffuse reflectance at source-detector separations close to one transport mean free path," J. Opt. Soc. Am. A **16**(12), 2935–2945 (1999).
5. P. R. Bargo, S. A. Prahl, T. T. Goodell, R. A. Sleven, G. Koval, G. Blair, and S. L. Jacques, "In vivo determination of optical properties of normal and tumor tissue with white light reflectance and an empirical light transport model during endoscopy," J. Biomed. Opt. **10**(3), 034018 (2005).
6. F. Bevilacqua, D. Piguet, P. Marquet, J. D. Gross, B. J. Tromberg, and C. Depeursinge, "In vivo local determination of tissue optical properties: applications to human brain," Appl. Opt. **38**(22), 4939–4950 (1999).
7. P. Thueler, I. Charvet, F. Bevilacqua, M. St. Ghislain, G. Ory, P. Marquet, P. Meda, B. Vermeulen, and C. Depeursinge, "In vivo endoscopic tissue diagnostics based on spectroscopic absorption, scattering, and phase function properties," J. Biomed. Opt. **8**(3), 495–503 (2003).
8. T. Lindbergh, E. Häggblad, H. Ahn, E. Göran Salerud, M. Larsson, and T. Strömberg, "Improved model for myocardial diffuse reflectance spectra by including mitochondrial cytochrome aa3, methemoglobin, and inhomogenously distributed RBC," J Biophoton. **4**(4), 268–276 (2011).
9. G. M. Palmer and N. Ramanujam, "Monte Carlo-based inverse model for calculating tissue optical properties. Part I: Theory and validation on synthetic phantoms," Appl. Opt. **45**(5), 1062–1071 (2006).
10. N. Haj-Hosseini, J. Richter, S. Andersson-Engels, and K. Wårdell, "Optical touch pointer for fluorescence guided glioblastoma resection using 5-aminolevulinic acid," Lasers Surg. Med. **42**(1), 9–14 (2010).

11. H. J. van Staveren, C. J. Moes, J. van Marie, S. A. Prahl, and M. J. van Gemert, "Light scattering in Intralipid-10% in the wavelength range of 400-1100 nm," Appl. Opt. **30**(31), 4507–4514 (1991).
12. T. Lindbergh, I. Fredriksson, M. Larsson, and T. Strömberg, "Spectral determination of a two-parametric phase function for polydispersive scattering liquids," Opt. Express **17**(3), 1610–1621 (2009).
13. L. Wang and S. L. Jacques, "Error estimation of measuring total interaction coefficients of turbid media using collimated light transmission," Phys. Med. Biol. **39**(12), 2349–2354 (1994).
14. S. N. Kasarova, N. G. Sultanova, C. D. Ivanov, and I. D. Nikolov, "Analysis of the dispersion of optical plastic materials," Opt. Mater. **29**(11), 1481–1490 (2007).
15. G. M. Hale and M. R. Querry, "Optical constants of water in the 200-nm to 200-μm wavelength region," Appl. Opt. **12**(3), 555–563 (1973).
16. H. Karlsson, A. Pettersson, M. Larsson, and T. Stromberg, "Can a one-layer optical skin model including melanin and inhomogeneously distributed blood explain spatially resolved diffuse reflectance spectra?" Proc. SPIE **7896**, 78962Y, 78962Y-9 (2011).
17. L. O. Reynolds and N. J. McCormick, "Approximate two-parameter phase function for light-scattering," J. Opt. Soc. Am. **70**(10), 1206–1212 (1980).
18. I. Fredriksson, M. Larsson, and T. Stromberg, "Inverse Monte Carlo in a multilayered tissue model for diffuse reflectance spectroscopy," J. Biomed. Opt. **17**, 047004 (2012).
19. T. Lindbergh, M. Larsson, Z. Szabó, H. Casimir-Ahn, and T. Strömberg, "Intramyocardial oxygen transport by quantitative diffuse reflectance spectroscopy in calves," J. Biomed. Opt. **15**(2), 027009 (2010).
20. R. L. van Veen, W. Verkruysse, and H. J. Sterenborg, "Diffuse-reflectance spectroscopy from 500 to 1060 nm by correction for inhomogeneously distributed absorbers," Opt. Lett. **27**(4), 246–248 (2002).
21. N. Rajaram, A. Gopal, X. Zhang, and J. W. Tunnell, "Experimental validation of the effects of microvasculature pigment packaging on in vivo diffuse reflectance spectroscopy," Lasers Surg. Med. **42**(7), 680–688 (2010).
22. I. Fredriksson, M. Larsson, and T. Stromberg, "Accuracy of vessel diameter estimated from a vessel packaging compensation in diffuse reflectance spectroscopy," Proc. SPIE **8087**, 80871M, 80871M-8 (2011).
23. A. Amelink, H. J. Sterenborg, J. L. Roodenburg, and M. J. Witjes, "Non-invasive measurement of the microvascular properties of non-dysplastic and dysplastic oral leukoplakias by use of optical spectroscopy," Oral Oncol. **47**(12), 1165–1170 (2011).

1. Introduction

The human tissue contains chromophores that absorb light with distinct spectroscopic patterns [1]. This includes the physiologically interesting molecule *heme* that has an absorption spectrum that strongly depends on its oxygenation status. By quantifying the amount of oxygenized and reduced heme the tissue fraction blood and its saturation can be estimated. However, when studying the diffusely backscattered light from an illuminated tissue the detected intensity depends not only on the amount of absorbing compounds but also on the amount of tissue scattering. As a consequence there is no bio-optical technique that directly measures the amount of tissue chromophores without taking into account tissue scattering.

To fully understand the combined effect of tissue scattering and absorption, the field of biomedical optics has devoted a lot of attention to methods for describing photon propagation in tissue. This research includes mathematical light scattering models that can predict the amount of detected light, given a predefined set of optical properties. By using the diffusion approximation both single- and multi-layered tissue models have been presented [2,3]. These models have proven successful in describing the amount of backscattered light far away from the injection point while failing at distances shorter than a few transport mean free paths [4]. One way to overcome this limitation is to use an empirical light scattering model [5]. A major disadvantage when using this approach is the need for an extensive calibration procedure using a set of well-known optical phantoms. By instead using Monte Carlo simulations to model photon propagation, the need for calibration can be limited to a single calibration measurement. However, this requires that the detector geometry is well-known.

With an accurate light scattering model it is possible to predict the amount of detected light, given a predefined set of optical properties. However, to estimate the amount of absorbing and scattering compounds in a tissue volume the inverse problem needs to be solved. Commonly, for a steady-state diffuse reflectance setup two different strategies have been used to solve this. The first approach involves an initial estimation of the reduced scattering coefficient and the absorption coefficient based on a measurement of the spatially resolved diffuse reflectance [6,7]. This strategy enables the estimation of the optical properties

without any wavelength dependent assumptions. However, to decompose the total absorption coefficient into quantitative amounts of specific tissue chromophores, an assumption regarding which chromophores to include and their absorption spectra is needed. For the second approach this assumption is included directly in the inverse solution. By also constraining the spectral appearance of the reduced scattering coefficient, the amount of tissue chromophores and the reduced scattering coefficient can be quantified using a single detector [5,8,9].

The second approach with a single detector setup has so far only been evaluated using an absolute calibration scheme. In a real measurement setup this is difficult to achieve as variations in the intensity of the illuminating light source or degradation of the calibration standard can occur. Likewise, an accurate characterization of the calibration standard is far from trivial to attain. These limitations can potentially be overcome by using a spatially resolved detector setup where a simplified inter-channel calibration scheme is used. This would remove both the need for a well-defined and stable calibration standard and the sensitivity to light source intensity variations.

The aim of this study was to quantify the effect of different Monte Carlo based light transport models and calibrations schemes on the quantification of absorption and scattering using a multi-distance fiberoptic spectroscopy probe. This was realized by evaluating the phase function of the scattering medium (Gegenbauer kernel or Henyey-Greenstein), the calibration method (absolute or relative calibration) and the number of included detector distances (4, 2 or 1 distance). The performance was evaluated using ten liquid optical phantoms containing a fix scattering level with different amount of absorbing compounds. Criteria for the evaluation were accuracy in estimation of the concentration of absorber, the scattering parameters and the magnitude and systematic appearance of residual spectra.

2. Material and methods

2.1 Optical phantoms

Five scattering phantoms, containing various proportions of Intralipid 20% and deionized water were prepared for the calculation of the scattering phase function (phantoms 1-5). The concentration of Intralipid in phantom 1 was approximately 10%, in phantom 2 approximately 5% (by diluting phantom 1), in phantom 3 2.5% (by diluting phantom 2) and so on. The fluorescence of diluted Intralipid was investigated by using a pulsed laser emitting at 405 nm [10], and the fluorescence found in the 500-900 nm wavelength range was negligible.

The scattering coefficient μ_s of each Intralipid dilution was determined using a spectral collimated transmission (SCT) setup, assuming the absorption to be negligible comparing to the scattering [11]. For the five phantoms μ_s ranged from 8.5 mm^{-1} to 0.57 mm^{-1} at 650 nm.

One additional non-absorbing Intralipid dilution (phantom 6) with approximately 10% of Intralipid was prepared. This dilution contained exactly the same amount of scattering compounds as in the ink dilutions described below (phantoms 7-16). Phantom 6 attained a μ_s of 7.1 mm^{-1} at 650 nm.

Before mixing the ink phantoms, two base absorber components were prepared by diluting the highly concentrated red and blue food dyes (Dr Oetker, Germany) with deionized water. The absorption coefficient μ_a for the two base components was calculated using SCT data. These absorption coefficients were later used in Eq. (7) as the base absorption spectra for the two chromophores. The attained $\mu_{a,red}$ was 3.5 mm^{-1} at 520 nm and the $\mu_{a,blue}$ was 3.6 mm^{-1} at 630 nm. The food dyes were assumed to be purely absorbing solutions as during the SCT no scattered light was visibly observed. The absorption spectra for the red and the blue dye dilutions were also close to zero for longer wavelengths which indicate that no scattering was present. The water absorption displayed no effect on the estimation of chromophore concentrations or the scattering parameters and was hence omitted from the model.

With the use of the absorbing base components, ten additional phantoms with physiologically relevant optical properties were created (phantoms 7-16). All with the same scattering coefficient, but with varying proportions of diluted red and blue food dye according to Table 1. The total size of every phantom was 100 ml mixed in 250 ml plastic cups with a diameter of ~5 cm. The optical properties of phantoms 7-16 are summarized in Table 1.

Table 1. Optical Phantoms 7-16 with Both Scattering and Absorption Components Included

Phantoms	Calculated μ_s [mm^{-1}] @650nm	Blue base component [%]	$\mu_{a,blue}$ [mm^{-1}] @630nm scaled from base component	Red base component [%]	$\mu_{a,red}$ [mm^{-1}] @520nm scaled from base component
7	7.1	25	0.90	-	-
8	7.1	6.25	0.23	-	-
9	7.1	1.5625	0.056	-	-
10	7.1	-	-	25	0.88
11	7.1	-	-	6.25	0.22
12	7.1	-	-	1.5625	0.055
13	7.1	25	0.90	25	0.88
14	7.1	25	0.90	6.25	0.22
15	7.1	6.25	0.23	25	0.88
16	7.1	6.25	0.23	6.25	0.22

2.2 Spectral collimated transmission

For the food dyes, the Intralipid and for all phantoms; μ_a, μ_s and the total attenuation coefficient μ_t were determined using spectral collimated transmission (SCT). A sample of ~5 ml for each phantom was illuminated with a broadband white light source (Avalight-HAL-S, Avantes BV, The Netherlands) and detected by a multi-channel spectrometer (AvaSpec 2048-5 RM, Avantes BV, The Netherlands, grating: VB 600 lines/mm). Optical glass fibers with a radius of 100 μm and a numerical aperture of 0.37 were used for light guiding. Two fiber optic collimators were attached to the fibers to ensure a collimated illumination of the sample and detection of the light passing through the sample [12]. For every sample, ten consecutive measurements with an increasing optical path length in the sample of 25 μm were performed. A maximum path length of 250 μm was chosen in order to not exceed three mfp (mean free path, $\text{mfp} = 1/(\mu_s + \mu_a)$ [13]). Measurements with intensity lower than 1% of the maximal detectable intensity for any wavelength were dismissed. The wavelength range used was limited to 500 to 900 nm.

2.3 Spatially resolved diffuse reflectance measurements

A fiber optic probe was used for the illumination of the phantoms and for the detection of the backscattered light during the spatially resolved diffuse reflection (SRDR) measurements. The probe consisted of one emitting fiber and four detecting fibers (ρ_{1-4}). The source-detector distances were 0.22 mm, 0.46 mm, 0.68 mm and 1.13 mm, respectively. The distances were measured using a microscope with a precision of ± 0.004 mm. The same light source, spectrometer and fiber settings used in the SCT measurements were also used in the SRDR setup. The integration time varied between 25 and 150 ms depending on the composition of the phantom. During the SRDR measurements, the probe was submerged approximately 1 cm into the phantom. For all SRDR measurements, an average over 5 s was analyzed.

2.4 Calibration of the system

All SRDR measurements were dark-corrected and white normalized. The white reference spectrum was collected from a barium-sulphate covered surface. Two different approaches of calibration were performed and evaluated: an absolute and a relative calibration of the system. The absolute calibration links the simulated spectra at all detector distances to the corresponding measured spectra by an independent calibration using polystyrene microspheres. For the relative calibration the different detector distances are calibrated to the same intensity by uniform illumination.

For the absolute calibration, SRDR spectra from a polystyrene microsphere solution (Bangs Laboratories, Inc., USA) were compared to Monte Carlo (MC) simulated spectra. The MC simulations were performed using an emitting/detecting layer (z>0) with a refractive index of 1.58 and a numerical aperture of 0.37, and a semi-infinite turbid layer (z<0) with a refractive index of 1.33. The optical properties of the turbid layer was given by the μ_s from the SCT measurements, $\mu_a = 0$ mm^{-1} and a Mie phase function. The Mie phase function was calculated using a wavelength resolved refraction index of water and polystyrene [14,15].

According to the manufacturer the microspheres had a nominal radius of 160 nm. To increase the precision in this measure, additional simulations were performed using a sphere radius ranging from 140 nm to 160 nm in steps of 5 nm. The radius generating the best fit to the measured spectra was chosen as the correct sphere size. At least 3.4E7 photons were simulated for the optimal sphere size.

The absolute calibration factors A_{abs} were calculated for each fiber as the mean ratio between measured spectra, $I_{meas,\ \mu\text{-sphere}}$, and simulated spectra, $I_{MC,\ \mu\text{-sphere}}$ according to [12]

$$A_{abs}(\rho) = \left\langle \frac{I_{meas,\ \mu\text{-sphere}}(\lambda,\rho)}{I_{MC,\ \mu\text{-sphere}}(\lambda,\rho)} \right\rangle_{\lambda}.$$

(1)

An absolute calibration of measured spectra from each of the phantoms was then obtained by

$$I_{abs}(\lambda,\rho) = \frac{I_{meas}(\lambda,\rho)}{A_{abs}(\rho)}.$$

(2)

The relative calibration factors were obtained from a measurement where all fibers were uniformly illuminated ($I_{meas,\ u.i.}$) using an integrating sphere connected to an external light source [16]. The relative calibration factors A_{rel} were calculated for each fiber as

$$A_{rel}(\rho) = \left\langle \frac{I_{meas,\ u.i.}(\lambda,\rho)}{\langle I_{meas,\ u.i.}(\lambda,\rho) \rangle_{\rho}} \right\rangle_{\lambda \in [500,630]}.$$

(3)

The wavelength range chosen was based on full width at half maximum for the un-normalized spectra. A relative calibration of measured spectra was obtained by

$$I_{rel}(\lambda,\rho) = \frac{I_{meas}(\lambda,\rho)}{A_{rel}(\rho)}.$$

(4)

2.5 Scattering phase function

Two different scattering phase functions for Intralipid 20% were considered: the Gegenbauer kernel (GK) phase function and the Henyey-Greenstein (HG) phase function. The GK phase function was described by two wavelength resolved parameters, $g_{GK}(\lambda)$ and $a_{GK}(\lambda)$, while

the HG phase function was defined by a single parameter, the anisotropy factor g (constant for all wavelengths).

The GK phase function parameters were estimated by finding the MC model that generated spectra with a minimal difference to the measured SRDR spectra using an inverse MC algorithm. In the iterative solution to this problem, the simulated spectra were generated using linear interpolation in a multi-dimensional look-up table containing pre-simulated intensities. The MC simulations were performed using an emitting/detecting layer (z>0) with a refractive index of 1.58 and a numerical aperture of 0.37, and a semi-infinite turbid layer (z<0) with a refractive index of 1.33. The look-up table covered a relevant range of g and a_{GK} values and was generated using $\mu_a = 0$ and $\mu_s(\lambda)$ values from the SCT measurement of the corresponding phantom. At least 3.6E7 photons were simulated for each phase function parameter. The inverse problem was solved for absolute calibrated SRDR-spectra from five phantoms (phantoms 1-5) that only contained Intralipid and deionized water using a trust-region-reflective optimization algorithm. The parameter $g_{GK}(\lambda)$ was calculated from the optimal a_{GK} and g [17].

In the optimization algorithm, starting values in the center of the simulated values were chosen i.e. $a_{GK} = 0.875$ and $g = 0.725$. Boundary constraints on the algorithm were given based on the limitations in the simulation grid. The error function to minimize was given by

$$E(a_{GK}, g) = \frac{I_{MC}(a_{GK}, g, \lambda, \text{phantom}, \rho)}{I_{abs}(\lambda, \text{phantom}, \rho)} - 1.$$

(5)

The optimization was done for each wavelength independently, resulting in an optimal solution ($a_{GK}^*(\lambda)$, $g^*(\lambda)$). A more detailed description for calculating the phase functions is described elsewhere [12].

For the HG phase function ($a_{GK} = 0.5$) a fixed value of $g = 0.7$ was used for all wavelengths.

2.6 Models

A four parameter model was used to generate simulated SRDR spectra. Two parameters, α and β, described the reduced scattering coefficient $\mu_s'(\lambda)$ as

$$\mu_s'(\lambda) = \alpha \cdot \left(\frac{\lambda}{650}\right)^{-\beta},$$

(6)

and two parameters, c_{blue} and c_{red} described the concentration of the chromophores. The absorption coefficient was defined as:

$$\mu_a(\lambda) = c_{blue} \cdot \mu_{a,blue}(\lambda) + c_{red} \cdot \mu_{a,red}(\lambda).$$

(7)

Depending on the chosen phase function (GK or HG) different values of the scattering coefficient were obtained from

$$\mu_s(\lambda) = \frac{\mu_s'(\lambda)}{1 - g},$$

(8)

where g is wavelength resolved for the GK phase function and fixed for the HG phase function.

The generation of MC simulated spectra for a given set of optical parameters was done using linear interpolation and look-up tables. This algorithm was similar to that used in the

GK phase function estimation, but with one exception. The look-up tables were generated using the estimated GK or the assumed HG phase function while covering a range of μ_a and μ_s values. Simulations were performed to attain 99 levels of μ_a, logarithmically distributed between 10^{-2} and $10^{1.5}$ (a zero value was included as a separate value resulting in 100 levels of μ_a) and 200 levels of μ_s linearly distributed between 0.1 and 20. At least 3.6E7 photons were traced in each simulation.

Seven models with different combinations of phase functions, calibration methods and number of included detectors, were evaluated. The models are summarized in Table 2.

Table 2. Summary of the Seven Models

Model	Phase function	Number of included detectors	Calibration method
1	GK	4	Absolute
2	GK	4	Relative
3	HG	4	Absolute
4	HG	4	Relative
5	HG	2[a]	Relative
6	HG	1[b]	Absolute
7	HG	1[b]	Relative

[a] Evaluated for $\rho = [0.46, 1.13]$

[b] Evaluated for all four detector distances

2.7 Data analysis

Due to imperfections in the measurement system, the phantom mixing and in the calibration methods, a variation in the intensity level in the wavelength range of 750 to 850 nm was found for all phantoms with the same scattering properties i.e. phantoms 6-16. In this wavelength range only the scattering affects the intensity and should be constant for all phantoms with the same scattering coefficient. A maximum intensity variation of 10% was found for the shortest source-detector distance. The effect of the intensity variation could also be seen in the optimized spectra as a systematic deviation between measured and simulated spectra, and in the residual as an offset and a systematic behavior. When the misfit was not handled, the algorithm compensated for the deviation by including non-existing chromophores in some of the phantoms. To account for this systematic deviation, an intensity relaxation parameter, q, was introduced in the optimization algorithm. For absolute calibrated spectra, q was defined as

$$q_{abs}(\rho) = \left\langle \frac{I_{MC}(\mu_a, \mu_s, \lambda, \rho)}{I_{abs}(\lambda, \rho)} \right\rangle_\lambda,$$

(9)

and for relative calibrated spectra as

$$q_{rel}(\rho) = \left\langle \frac{I_{MC}(\mu_a, \mu_s, \lambda, \rho)}{I_{rel}(\lambda, \rho)} \cdot \left\langle \frac{I_{MC}(\mu_a, \mu_s, \lambda, \rho)}{I_{rel}(\lambda, \rho)} \right\rangle_{\lambda,\rho}^{-1} \right\rangle_\lambda.$$

(10)

The parameter, q, was limited to only allow for $\pm 10\%$ intensity variation for each detector distance ($0.9 \leq q(\rho) \leq 1.1$). For single-detector data (model 6 and 7) no relaxation was applied ($q(\rho) = 1$).

For all seven models, the concentration of the two chromophores in the ten phantoms was calculated by using a trust-region-reflective algorithm to minimize the error between

simulated and measured SRDR spectra for all phantoms. The error function for absolute calibration in Eq. (11) depended on the four parameters; α, β, c_{blue} and c_{red},

$$E_{\text{abs}}(\alpha,\beta,c_{\text{blue}},c_{\text{red}}) = \frac{I_{\text{MC}}(\mu_{\text{a}},\mu_{\text{s}},\lambda,\rho)}{q_{\text{abs}}(\rho) \cdot I_{\text{abs}}(\lambda,\rho)} - 1, \tag{11}$$

where the relationships between α, β, g and $\mu_{\text{s}}(\lambda)$ are given in Eq. (6) and Eq. (8) and the relationship between c_{blue}, c_{red} and $\mu_{\text{a}}(\lambda)$ is given in Eq. (7). The parameter q is calculated for each iteration in the optimization algorithm. The error function for relative calibration was defined as

$$E_{\text{rel}}(\alpha,\beta,c_{\text{blue}},c_{\text{red}}) = \frac{I_{\text{MC}}(\mu_{\text{a}},\mu_{\text{s}},\lambda,\rho)}{q_{\text{rel}}(\rho) \cdot I_{\text{rel}}(\lambda,\rho)} \cdot \left\langle \frac{I_{\text{MC}}(\mu_{\text{a}},\mu_{\text{s}},\lambda,\rho)}{I_{\text{rel}}(\lambda,\rho)} \right\rangle_{\lambda,\rho}^{-1} - 1. \tag{12}$$

All wavelengths of the measured SRDR spectra with intensity lower than 1% of the maximal detectable intensity were excluded from influencing the error. The optimization resulted in: α^{*}, β^{*}, c_{blue}^{*}, c_{red}^{*}.

2.8 Model evaluation

The seven models were evaluated regarding the accuracy in the estimation of the chromophore concentration and in the estimation of the reduced scattering coefficient. The rms-values and the systematics of the residual spectra were also evaluated.

The accuracy for the models in estimating the chromophore content was calculated as the sum of the difference between true and estimated chromophore concentration, divided by the sum of true chromophore concentration:

$$E_{\text{chrom}} = \frac{\displaystyle\sum_{chromophore} \left| c_{\text{blue/red}} - c_{\text{blue/red}}^{*} \right|}{\displaystyle\sum_{chromophore} c_{\text{blue/red}}}. \tag{13}$$

The accuracy of the estimated reduced scattering coefficient was given by the rms-error between $\mu_{\text{s}}'(\lambda)$ for phantom 6, calculated from the scattering phase function and $\mu_{\text{s}}(\lambda)$ from SCT, and the modeled reduced scattering coefficient ($\hat{\mu}_{\text{s}}'(\lambda) = \alpha^{*}(\lambda/650)^{-\beta^{*}}$). The scattering error, E_{scatt} was calculated for every model and phantom as

$$E_{\text{scatt}} = \left(\left\langle \left(\frac{\mu_{\text{s}}'(\lambda)}{\hat{\mu}_{\text{s}}'(\lambda)} - 1 \right)^{2} \right\rangle_{\lambda} \right)^{1/2}. \tag{14}$$

The rms-value of the residual spectra was

$$E_{\text{resid}} = \left(\left\langle E_{\text{abs/rel}}^{2}(\alpha^{*},\beta^{*},c_{\text{blue}}^{*},c_{\text{red}}^{*}) \right\rangle_{\lambda} \right)^{1/2}. \tag{15}$$

2.9 Statistical comparisons

The results from data analysis of spectra from phantoms 7-16 were statistically compared regarding the chromophore concentration error (E_{chrom}), the scattering coefficient error (E_{scatt} using the results from phantom 6 as reference value), and the rms-value of the residual spectra (E_{resid}). Models using a different number of source detector distances were not compared

regarding E_{resid} , since it can be expected that fewer distances will yield a better spectral fit. The statistical comparisons were done using the Wilcoxon matched pairs test and Statistica 10 (StatSoft Inc).

3. Results

3.1 Spectral collimated transmission

To validate the expected theoretical value of the total attenuation coefficient (μ_t ; $\mu_t = \mu_a + \mu_s$), SCT measurements were performed for phantoms 7-16. The maximum deviation at any wavelength, between expected theoretical value and measured was 1.4% (mean 0.7%).

3.2 Calibration of the system

The estimated size of the microspheres was chosen as when corresponding simulated and measured spectra in the shortest source-detector distance (with the most characteristic spectra) had coinciding minima (Fig. 1). In this case, the best fit was the simulation of microspheres with a radius of 150 nm (see Fig. 1).
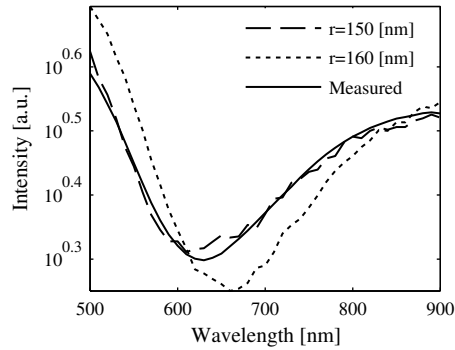

Fig. 1. Measured spectra from a microsphere solution for the shortest detector distance (solid black) compared to simulated spectra for spheres with a radius of 150 nm (dashed black) and simulated spectra for spheres with a radius of 160 nm (dotted black).

The calibration factors from the absolute and the relative calibration method, divided by their mean value, differed less than 6%.

3.3 Phase function

For the approximation of the GK phase function, the wavelength resolved a_{GK} ranged between 1.27 and 0.74. The anisotropy factor g for phantom 6 is shown in Fig. 2. The corresponding reduced scattering coefficient calculated from Eq. (8) and Eq. (6) for phantom 6 resulted in $\alpha = 1.99$ and $\beta = 1.05$.
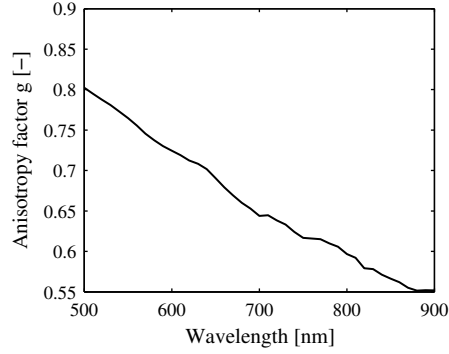
Fig. 2. The estimated wavelength resolved anisotropy factor for the Gegenbauer kernel phase function.

3.4 Validation of q

The inclusion of the intensity relaxation (q) in the optimization algorithm was evaluated both in the absolute calibrated case and in the relative calibrated for phantoms 7-16 with a GK phase function. Without q, systematic residuals were found for both absolute (Fig. 3) and relative calibrations (models 1 and 2).
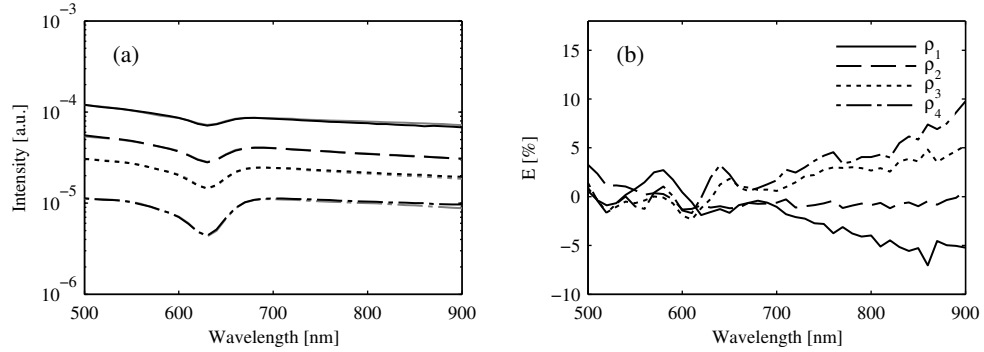

Fig. 3. (a) Measured (black; model 1 without q) and simulated spectra (gray) for the four detector distances in absolute calibrated phantom 8. (b) The residual.

The inclusion of q significantly improved E_{scatt} and E_{resid} for model 1 (Fig. 4) and 2 ($p < 0.01$), and E_{chrom} for model 1 ($p < 0.05$).
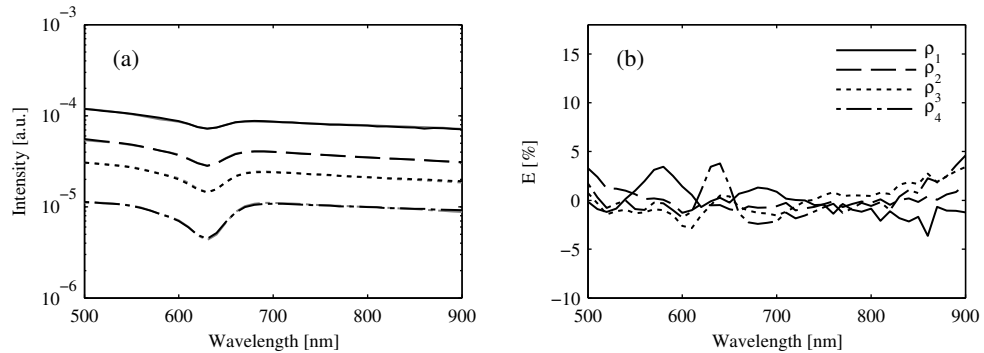

Fig. 4. (a) Measured (black; model 1 with q) and simulated spectra (gray) for the four detector distances in absolute calibrated phantom 8. (b) The residual.

3.5 Model performance

The performance of the seven models regarding chromophore estimation, scattering coefficient estimation, rms-error and a systematic residual is summarized in Table 3. The intensity relaxation was used in all models, except in models 6 and 7.

Table 3. Performance of the Seven Models

Model	Summary (phase function, #detectors, calibration method)	$\langle E_{\mathrm{chrom}} \rangle_{phantom}$ [%], chromophore estimation	$\langle E_{\mathrm{scatt}} \rangle_{phantom}$ [%], $\mu_s'(\lambda)$ estimation	E_{resid} [%]	Systematic residual (Yes/No)
1	GK, 4, abs.	7.7	4.7	2.1	N
2	GK, 4, rel.	9.9	7.7	2.1	N
3	HG, 4, abs.	8.6	6.2	3.0	Y
4	HG, 4, rel.	8.5	8.2	3.1	Y
5	HG, 2, rel.	6.8	8.3	2.0	Y
6	HG, 1, abs.	40.6; 11.6; 7.7; 8.2[a]	7.0; 5.0; 8.3; 13.6[a]	1.1; 0.8; 1.1; 1.5[a]	N
7	HG, 1, rel.	45.8; 13.6; 10.7; 9.7[a]	160; 31.3; 24.3; 28.5[a]	0.9; 0.7; 0.9; 1.4[a]	N

[a] Calculated for each of the four detector distances, shortest to longest.

The effect of the phase function was assessed firstly by comparing models 1 and 3 (GK vs. HG for absolute calibrated spectra). Model 1 had significantly lower E_{resid} ($p < 0.01$). Model 3 was producing a systematic residual spectrum. Figure 4 shows the fitting of model 1 for phantom 8 and Fig. 5 the fitting of model 3 for phantom 8.
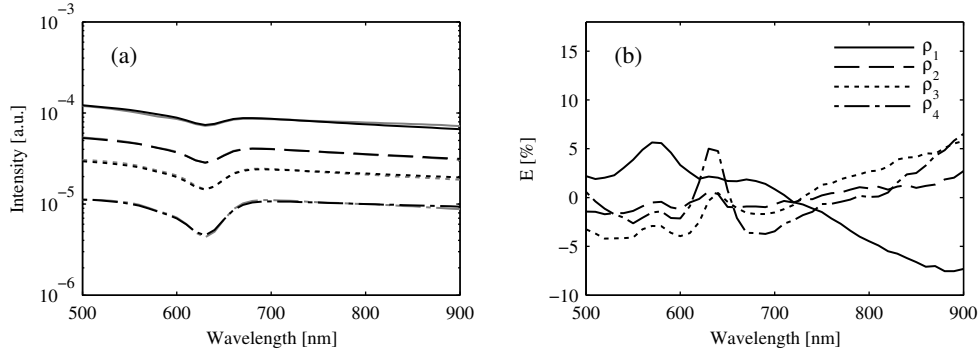

Fig. 5. (a) Measured (black; model 3 with q) and simulated spectra (gray) for the four detector distances in absolute calibrated phantom 8**.** (b) The residual.

Secondly, models 2 and 4 were compared (relative calibration). A HG phase function produced a systematic residual and a significantly poorer E_{resid} (p < 0.01) than the GK phase function.

The effect of the calibration method was assessed using the HG phase function by comparing models 3 and 4 (absolute calibrated vs. relative calibrated). There were no significant differences in any parameter. A similar comparison between models 1 and 2 showed that absolute calibration gave significantly better E_{chrom} and E_{scatt} (p < 0.05).

When comparing model 4 and model 5, where model 5 had a reduced number of included detector distances, there were no significant differences in any parameter. Figure 6 shows the fit for model 5 on phantom 11.
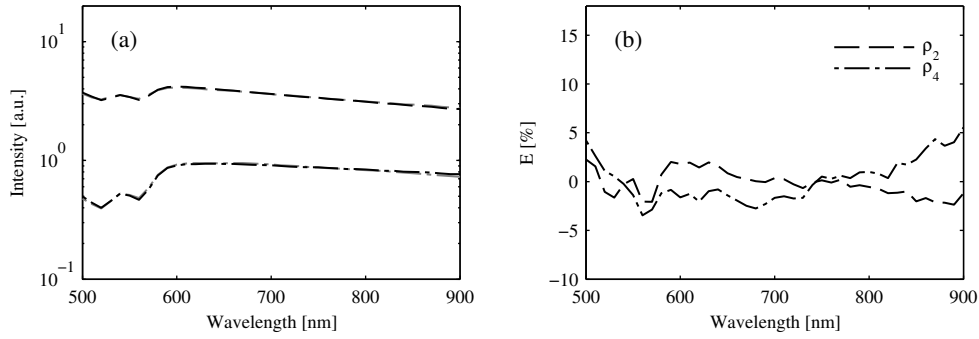
Fig. 6. (a) Measured (black; model 5 with q) and simulated spectra (gray) for the two detector distances in relative calibrated phantom 11. (b) The residual.

For some of the detector separations, the sixth model with only one absolute calibrated detector fiber showed significantly poorer E_{chrom} (p < 0.01 (ρ_1)) and significantly poorer E_{scatt} (p < 0.01 (ρ_1, ρ_4), p < 0.05 (ρ_3)) than model 1. For ρ_2, however, no significant differences were found in E_{chrom} or E_{scatt}. The seventh model with only one relative calibrated detector fiber had significantly poorer E_{chrom} (p < 0.05 (ρ_1, ρ_2) and significantly poorer E_{scatt} (p < 0.01 (all ρ_i)) than model 1.

When comparing models 1 and 5, no significant differences were found in E_{chrom} or E_{scatt}. Table 4 shows the results from model 1 and model 5 in more detail.

Table 4. Calculated Model Errors of the Included Chromophores and the Reduced Scattering Coefficient for Model 1 and Model 5

	Phantom									
	7	*8*	*9*	*10*	*11*	*12*	*13*	*14*	*15*	*16*
E_{chrom} [%], model 1	1.8	9.5	19.0	6.9	3.3	24.5	2.8	2.2	3.8	3.2
E_{chrom} [%], model 5	1.1	6.8	7.3	8.6	0.8	18.5	5.7	3.2	7.0	9.0
E_{scatt} [%], model 1	0.2	3.3	3.9	7.0	3.5	2.7	9.4	7.7	4.3	4.6
E_{scatt} [%], model 5	6.5	11.7	10.1	6.4	12.2	15.3	3.8	3.9	8.2	4.7

4. Discussion

In summary, we have presented various light transport models for quantifying absorption and scattering in liquid optical phantoms using a fiberoptic probe with multiple detector distances in the 0.2-1.2 mm range. The models varied regarding scattering phase function, calibration method and included detector distances. Evaluation of the models was performed on ten optical phantoms with various amounts of scattering and absorbing compounds. Intralipid 20% was used as the scattering component and red and blue food dyes as the absorbing components. Monte Carlo simulations were performed to model the measured diffuse reflectance spectra from the phantoms. The intensity calibration for the detecting fibers was undertaken using either microspheres (absolute factors) or uniform illumination (relative factors between detectors). When the model included two or more detecting fibers, spectral fitting of phantoms was significantly improved by allowing for $\pm 10\%$ intensity relaxation in the optimization algorithm. For the multi-detector setups, non-systematic residual spectra was only found using the more complex Gegenbauer-kernel phase function with two wavelength dependent parameters, in comparison to using a Henyey-Greenstein phase function with constant anisotropy factor. The estimation of the concentration of absorbing dyes was similar

for all multi-detector models. Using a single detecting fiber demanded a source detector distance of 0.46 mm (the second smallest distance in this study) and an absolute calibration to estimate scattering and absorption levels with accuracy similar to the multi-detector setups.

4.1 Phase function

When comparing the GK and HG phase functions it should be noticed that the GK phase function resulted in non-systematic residual spectra, whereas systematic residual spectra were found when the HG phase function was used in the multi-detector models. However, it may be impossible to estimate a wavelength resolved GK phase function in more complex measurement situations than liquid phantoms. When comparing the models with a GK phase function with the models using a HG phase function there were no significant differences in the estimation of the included chromophores or the reduced scattering coefficient. Also, none of the models included an amount of a non-existing chromophore. The results indicate that a model with a HG phase function with a constant anisotropy factor is sufficient for accurate chromophore content and reduced scattering coefficient estimation. However, when using spectroscopy in human tissue where the true chromophore concentration is not known, a systematic residual can be used as a powerful tool in determining different spectral analysis models [8].

4.2 Calibration method

With an absolute calibration method it is possible to get accurate estimations of both the absorption and the scattering using only one detector distance. Yet, the absolute calibration procedure is complex to perform and a sufficient accuracy and consistency over time in the calibration factors might be hard to accomplish. The microspheres used in the absolute calibration method have to be stored and handled correctly. With a relative calibration method it is possible to carry out a calibration by much simpler means. Furthermore, common errors in the different channels e.g. intensity variations in the lamp are eliminated with a relative calibration. The drawback is the need for multiple detector distances, since the scattering cannot be estimated accurately with only one relative calibrated distance.

A major finding in this study is that applying an intensity relaxation (q), allowing for small errors in the calibration factors or other measurement imperfections, significantly improved all evaluated parameters (absorption, scattering accuracy, the magnitude and randomness of the residual spectra). The allowed variation in the intensity was determined based on measurements on multiple similar optical phantoms. Without any limitations on q, the models failed to converge for some phantoms.

4.3 Number of source detector distances in model

Due to the short source-detector distance for the first detector distance, implying a short photon path length, almost no information is provided in the SRDR spectra regarding the chromophore content. This is observed in Table 3 when trying to fit measured spectra from only the first detector distance in models 6 and 7, resulting in a large error in the chromophore estimation comparing fitting to the other detector distances. When choosing the included distances in model 5, the shortest distance is discarded due to the lack of information and the second and the last are chosen in order to have two well separated distances.

4.4 Clinical implications

The results of this study have implications for the use of diffuse reflectance spectroscopy as a quantitative tool in tissue diagnosis. The photon propagation model, however, needs to be adapted to the tissue under investigation. We have previously shown that a homogenous model cannot be used for explaining absolute calibrated spectra from skin tissue recorded at two source-detector separations (0.46 mm and 1.2 mm) [16]. With a three layer model,

mimicking the real structure of skin tissue, spectra at two source-detector separations can be modeled accurately [18].

When modeling tissue it is important that all significant chromophores are included. Otherwise, included chromophores will compensate for omitted ones, resulting in erroneous estimations [16,19]. In real tissue, light interaction with blood does only occur in vessels and not homogenously, which affects the diffusely reflected spectra. This is known as the vessel packaging effect and should be compensated for [20–23].

5. Conclusion

We have evaluated various light transport models and calibrations schemes for quantifying absorption and scattering in liquid optical phantoms. We found that no a-priori knowledge of the scattering phase function is necessary and that it is sufficient to use either two relative calibrated detector distances or one absolute calibrated detector at a separation of 0.46 mm.